A non-equilibrium transient phase revealed by *in situ* GISAXS tracking of the solvent-assisted nanoparticle self-assembly

Karol Vegso,[1] Peter Siffalovic,[1] Matej Jergel,[1] Martin Weis,[1] Eva Majkova,[1] Stefan Luby,[1] Ignac Capek,[2] Adeline Buffet[3] and Stephan V. Roth[3]

[1]Institute of Physics, Slovak Academy of Sciences, Dubravska cesta 9, 84511 Bratislava, Slovakia,

[2]Polymer Institute, Slovak Academy of Sciences, Dubravska cesta 9, 84541 Bratislava, Slovakia

[3]HASYLAB, DESY, Notkestrasse 86, Hamburg, 22603, Germany

Email address: karol.vegso@savba.sk

Keywords: Ag nanoparticles, solvent-assisted self-assembly, short-range to long-range order transition, grazing-incidence small-angle X-ray scattering

Abstract

We report on a time-resolved study of the colloidal nanoparticle self-assembly into a high-quality nanoparticle crystal with the face-centered cubic crystallographic symmetry. In particular, the grazing-incidence small-angle X-ray scattering technique was employed to track kinetics of the solvent evaporation driven self-assembly on casting a drop of plasmonic Ag nanoparticles on a silicon substrate. The short-range (cumulative) disorder typical for paracrystal structures before the complete solvent

evaporation at 300-350 s from the drop casting was found with the exception of the time window of 125-150 s where a highly regular transient phase with the long-range order was observed. This temporary improvement of the nanoparticle crystal perfection occurring shortly before the complete solvent evaporation is the main message of the paper. It is attributed to interaction between the surfactant shells of the neighboring nanoparticles getting into contact in the presence of solvent residua to the end of the solvent evaporation that results in a larger nanoparticle hydrodynamic diameter with a smaller dispersion and thus improvement of the crystallization. This process has direct impact on the quality of the resulting nanoparticle crystal and tailoring its properties.

Introduction

Colloidal plasmonic nanoparticles and their self-assembled two- and three-dimensional (2D, 3D) arrays (nanoparticle crystals) have been extensively studied in the last decade as promising structures for nanophotonics and biotechnology (Elbaz et al. 2013; Moscatelli 2012; Atwater and Polmann 2010). In particular, tailoring optical properties by the nanoparticle layout would enable us to circumvent diffraction limits of conventional optics (Rong et al. 2008; Maier et al. 2003; Willingham and Link 2011). Such an approach requires control of the nanoparticle size dispersion that is closely related to the plasmon bandwidth (Martin et al. 2010; Link and El-Sayed 1999) as well as control of the interparticle distances and crystallographic symmetry in the nanoparticle array that affect the dipole-dipole coupling between the neighboring nanoparticles (Macfarlane et al. 2011; Rupich et al. 2009). Typical methods for preparation of 2D nanoparticle arrays from colloidal solution are Langmuir-Schaefer (LS) and Langmuir-Blodgett (LB) techniques or the solvent-assisted self-assembly during drying a colloidal drop that was casted on a substrate (Martin et al. 2010; Smilgies et al. 2012; Pohjalainen et al. 2010; Smith et al. 2009). The air-water interface utilized in LS and LB techniques requires nanoparticles with a hydrophobic surfactant shell (Chitu et al. 2010; Vegso et al. 2012; Dai et al. 2013). For preparation of 3D nanoparticle arrays, the layer-by-layer deposition based on LS or LB technique or the solvent-assisted self-assembly may be employed (Chitu et al. 2010; Dunphy et al. 2008).

The solvent-assisted self-assembly seems to be the most attractive method for preparation of the nanoparticle arrays because of its simplicity and possibility to prepare nanoparticle arrays with various symmetries such as hexagonal, rhombohedral, face-centered cubic or body-centered cubic (Smilgies et al. 2012; Vegso et al. 2012; Dunphy et al. 2008; Altamura et al. 2012) depending on the external drying parameters. Therefore, major part of studies on the solvent-assisted nanoparticle self-assembly have been devoted to the effect of the external drying parameters such as ambient temperature, temperature of the substrate or evaporation rate on the crystallographic symmetry of the resulting 3D nanoparticle array (Dunphy et al. 2008). However, little is known about the self-assembly kinetics itself that gives a key to tailoring the optical properties of the nanoparticle array. This paper is devoted to a study of the solvent-assisted self-assembly kinetics of silver plasmonic nanoparticles by the time-resolved small-angle X-ray scattering at grazing incidence (GISAXS). To our best knowledge, such a study has not been performed yet. The GISAXS technique is unique as it provides statistical information inherently averaged over hundreds of micrometers with adjustable in-depth sensitivity in the nanometer range (Renaud et al. 2009)**.** In particular, build-up of the nanoparticle array in terms of the crystallographic symmetry, order perfection or interparticle distance can be tracked in real time down to millisecond resolution provided a fast 2D detector is used. Such a study cannot be done by direct optical imaging methods requiring vacuum (SEM, TEM) or scanning probe techniques that provide local information.

Experimental details

The silver nanoparticles were synthesized from silver nitrate precursor by a high-temperature solution phase reaction. The synthesis details can be found elsewhere (Vegso et al. 2011). The nanoparticles dissolved in toluene were stabilized with surfactant shells of oleylamine and oleic acid. The metallic core size of the nanoparticles of 6±0.6 nm was determined by the small-angle X-ray scattering of the colloidal solution. The pristine colloidal nanoparticle solution was at first dried completely. Subsequently, 10 mg of the dried silver nanoparticles were dissolved in 1 mL of toluene. In the final step, 10 μL of this colloidal nanoparticle solution was drop-casted on a silicon wafer of 20 mm × 20 mm

size by means of an automatic injector with container. Prior to application of the colloidal drop on the silicon wafer, the wafer was cleaned by polymer solution (First Contact) and subsequently put into an ozone-generating UV reactor (hv=4.9 and 6.7 eV) (Siffalovic et al. 2010). The *in-situ* time-resolved GISAXS measurements of the drying drop were performed at high-brilliance synchrotron radiation source Petra III at MINAXS beamline (DESY, Germany) (Buffet et al. 2012). The energy of X-ray photons was set to 12.65 keV (λ = 0.098 nm). The size of the X-ray beam was 60 (±1) μm × 40 (±1) μm in the horizontal and vertical directions, respectively. The total flux of the X-ray beam at the sample position was 5 (±1) × 10^{11} photon/s. In order to avoid radiation damage induced by the X-ray photons, an aluminum absorber of 0.5 mm nominal thickness (attenuation factor 0.19) was inserted into the X-ray beam path. The X-ray beam impinged on the sample surface at an angle of incidence of 0.7 deg. The components of the scattering vector $\boldsymbol{q}$ in the reciprocal space are defined as (Renaud et al. 2009)

$$q_x=k_0[\cos(2\Theta_f)\cos(\alpha_f)-\cos(\alpha_i)] \quad (1)$$

$$q_y= k_0[\sin(2\Theta_f)\cos(\alpha_f)] \quad (2)$$

$$q_z= k_0[\sin(\alpha_i)+\sin(\alpha_f)] \quad (3)$$

where α_i and α_f are the angles of incidence and exit defined in the plane normal to the sample surface, respectively, $k_0=(2\pi)/\lambda$, and $2\Theta_f$ is the exit angle defined in the plane parallel to the sample surface. In the GISAXS region, the magnitude of q_x coordinate is negligible with respect to the magnitude of q_y one, hence, (q_y, q_z) coordinates are sufficient to show the GISAXS patterns. A fast 2D silicon-based X-ray detector Pilatus 300K (Dectris, Switzerland) coupled to an automatic injector of the nanoparticle solution was used for measurement of a large series of GISAXS frames in the form of a movie. The exposure time of 0.5 s for one GISAXS frame was selected. For evaluation of the temporal evolution of GISAXS from the drying drop, series of 10 successive images were always integrated giving a resolution of 5 s. The *in-situ* GISAXS measurements of the drying drop were complemented by the *ex-situ* optical microscopy (VHX-500F, Keyence) and Rayleigh scattering measurements to visualize

surface topography of the dried nanoparticle droplet. The optical microscopy images were taken with 50× (Fig. 1a,b) and 300× (Fig. 1c) magnifications. The Rayleigh scattering was measured on a confocal Raman microscope (Alpha 300R, WiTec) where the notch filter blocking the excitation laser line (λ=532 nm) was removed. The imaging relies on visualization of the spatial distribution of the Rayleigh scattering line intensity over 100 μm × 100 μm area divided into 100 scanning lines where each line was sampled at 100 points (Fig. 2a). The lateral and depth resolutions of the microscope in the configuration used were ~300 nm and ~800 nm, respectively. The integration time for each Raman spectrum was set to 0.1 s. Finally in order to quantify the droplet surface profile in the normal direction, stylus profilometry (Dektak 150, Veeco) was applied.

Results and discussion

The optical microscopy images (Fig. 1) show the dried nanoparticle droplet of ~16 mm diameter located approximately in the centre of the 20 × 20 mm silicon wafer with concentric rings around the central stain. The droplet did not reach the substrate size, hence, the droplet wetting and subsequent solvent evaporation were not affected by the substrate margins. The mechanism of forming the ring deposits under these conditions was for the first time explained by Deegan et al. (Deegan et al. 1997) and was termed as the “coffee ring effect“. Briefly, the droplet surface patterning shown in Fig. 1 is the result of a repetitive pinning and depinning of the shrinking droplet contact line (Lin 2012). The droplet surface morphology was examined in more detail by Rayleigh scattering which revealed stripes corresponding to the ring deposits (Fig. 2a). Their cross-section (Fig. 2b) provides the full-width-at-half-maximum (FWHM) and full-width-at-tenth-of-maximum (FWTM) values of the ring deposits of 11.1 μm and 20.2 μm, respectively, while the height of the ring deposites determined by stylus profilometry (not shown) reaches only 0.1 μm. Hence, the aspect ratio of the ring modulations is very low, being just 0.005. In the *in-situ* GISAXS experiment, the X-ray beam propagated along A line depicted in Fig. 1b. Taking into account the X-ray beam dimensions and the ring size as given above, the nanoscale

GISAXS characterization of the nanoparticle crystal was performed exclusively in the region of the concentric ring deposits.

The initial GISAXS pattern on the drop casting (Fig. 3a) shows a pair of clearly visible diffraction spots in the plane of incidence of X-rays. These spots indicate stacking of the nanoparticle layers on the substrate that is periodic along the substrate normal and suggests that the nanoparticle layers are in contact from the very beginning of GISAXS measurements. Presumably, nanoparticle clusters were formed in the injector container after its filling up with the nanoparticle solution still before the drop casting. Actually, ~3 minutes were needed after filling up the container to inject remotely the solution and to start GISAXS measurements because of safety procedures (activation of interlocks, hutch closing). The absence of the diffraction spots out of the plane of incidence suggests that the nanoparticle positions inside the planes are uncorrelated. Hence, there is no 3D nanoparticle crystal immediately on the drop casting. The GISAXS pattern taken 120-125 s later (Fig. 3b) shows clearly visible diffraction spots out of the plane of incidence. The GISAXS pattern of the completely dried nanoparticle crystal (Fig. 3c) is similar, however, more diffuse scattering is visible outside the spots that is related to an increased disorder in the nanoparticle crystal. The distribution of the diffraction spots corresponds to a highly ordered nanoparticle crystal with the face-centered cubic (*fcc*) symmetry and [*111*] direction oriented parallel to the substrate normal (Figs. 3d, 4a). Hence, the crystal may be viewed as *ABC* stacking of hexagonally closed-packed nanoparticle layers (Fig. 4b). The lattice parameter of the *fcc* nanoparticle crystal derived from the indexed spots in the GISAXS pattern is $a = 11.9$ nm that gives the interparticle distance inside the hexagonally ordered layers $\Delta = \sqrt{2}/2a = 8.4$ nm and the interlayer distance $d_{111} = \sqrt{3}/3\ a = 6.9$ nm.

The evolution of *111* and *222* Bragg peaks obtained from integration of the GISAXS patterns around $q_y = 0$ nm^{-1} for selected times of the drop drying is depicted in Fig. 5a. The intensities of both Bragg peaks increase with drying time which suggests increasing the diffracting volume as the solvent evaporates and the self-assembly proceeds. On the other hand, there are no distinct changes of the Bragg

peak widths visible by a naked eye except for some broadening in the final state of the evaporated solvent at 300-305 s. The q_y diffraction profiles of the Bragg peaks out of the plane of incidence obtained from integration of the GISAXS patterns in selected intervals of q_z and time (Figs. 5b-d) emerge some 100-105 s after the start of the measurement when *ABC* stacking of the nanoparticle layers is established. Before, only broad modulations due to the nanoparticle form factor are visible. After evaporation of the residua of the organic solvent, highly ordered *fcc* nanoparticle crystal is formed.

In order to have a better insight into the changes of the Bragg peaks, the intensity profiles along q_z axis of *111* and *222* Bragg peaks measured at different times were normalized to the maximum intensity and plotted in separate graphs (Figs. 6a,b). A gradual narrowing of both peaks up to 120-125 s is observed suggesting an improvement of the stacking periodicity while the opposite takes place after 300-305 s. A direct comparison of the *111* and *222* Bragg peaks at different times (Figs. 6c-f) indicates approaching their widths during the peaks narrowing with the maximum overlap at 120-125 s (Fig. 6e) before the opposite trend is established (Fig. 6f). This evolution of Bragg peaks suggests a temporary transition of the short-range order to the long-range one in [*111*] direction during the solvent evaporation that culminates at 125 s. In the following, the effect will be analyzed within the paracrystalline model of the nanoparticle ordering.

The self-assembly kinetics can be monitored rigorously by quantification of *111* and *222* Bragg peaks. The area A_{111} under *111* Bragg peak as a function of time (Fig. 7a) grows rapidly after 100 s and comes to saturation after 150 s. This suggests an increased number of the nanoparticle layers contributing to the diffraction along [*111*] direction when the drying process proceeds from the drop margins to the drop centre. The interlayer distance $d_{111} = 2\pi/P_{111}$ (Fig. 7b) derived from P_{111} position of the *111* Bragg peak shows a small but important S-shaped instability of ≈0.1 nm amplitude at 100-155 s that is discussed further. The temporal evolution of the full width at half maximum (FWHM) of *111* and *222* Bragg peaks (Fig. 7c) in the interval of 0-100 s shows that the latter peak is broader. Such a Bragg peak broadening with increasing diffraction order is typical for the short-range ordered (paracrystalline)

structures. Here, position of a nanoparticle inherits disorder from the nanoparticle neighbors, hence, disorder propagates in a cumulative way. In the interval of 100-150 s, FWHM values of both Bragg peaks exhibit dips that are mutually shifted in time. Consequently, FWHM of *222* Bragg peak approaches temporarily that of *111* one as it can be seen in Fig. 8. This suggests that in the interval of 125-155 s, the nanoparticle crystal transforms from a short-range ordered to a long-range ordered structure where the nanoparticle positions are distributed around the lattice points of space lattice with Gaussian probability. This is in line with an increased size of the coherently scattering domains in [*111*] direction derived from FWHM of *111* Bragg peak as $\Pi = 2\pi/\mathrm{FWHM}$ (Fig. 7d). After 155 s, the short-range order is re-established before the solvent is completely evaporated at 300-350 s.

The FWHM of a diffraction peak with Gaussian shape in the short-range ordered structure obeys the relation (Hindeleh and Hosemann 1988; Eads and Millane 2001)

$$\mathrm{FWHM}^2 = 4\pi^2\left[\left(\frac{\pi^2 n^2 g^2}{d}\right)^2 + \left(\frac{1}{Nd}\right)^2\right] \tag{4}$$

where n is the diffraction order, g is the degree of disorder of the short-range ordered crystal, N is the number of the lattice planes contributing to a particular diffraction (domain size) and d is the interplanar spacing along the considered crystallographic direction. In our case, $n = 1$ and 2 for *111* and *222* Bragg peaks, respectively, N means the number of layers contributing to the diffraction in [*111*] direction and d is the interlayer distance d_{111}. For $g = 0$, FWHM values of *111* and *222* Bragg peaks are equal and controled solely by $1/Nd$ which is the case of a perfect long-range ordered structure. The Eq. 4 enables us to calculate the degree of disorder g and the domain size N along [*111*] direction from FWHM values of *111* and *222* Bragg peaks and the interlayer distance d_{111} as

$$g = \frac{\sqrt{d_{111}}}{\pi\sqrt{\pi}}\sqrt{\frac{\mathrm{FWHM}_{222}^2 - \mathrm{FWHM}_{111}^2}{60}} \tag{5}$$

$$N = \frac{\sqrt{60\pi}}{d_{111}\sqrt{16\mathrm{FWHM}_{111}^2 - \mathrm{FWHM}_{222}^2}} \quad (6)$$

where FWHM_{111} and FWHM_{222} refer to *111* and *222* Bragg peaks, respectively. The temporal evolution of the degree of disorder and the domain size along [*111*] direction derived from Eqs. 5, 6 is shown in Fig. 9. In the interval of 0-100 s, both parameters take up nearly constant values of ≈3.4 % and 15 layers for the degree of disorder and the domain size, respectively. When the crystal transforms from the short-range to the long-range ordered structure in the interval of 125-155 s, the degree of disorder drops to 2 % and the domain size increases to 18 layers. Later on, the evolution is reversed and saturates at 3 % for the former and 15 layers for the latter parameter. The temporal evolution of the domain size derived from the short-range order model (Fig. 9b) agrees well with that derived from FWHM of *111* Bragg peak (Fig. 7d). Another supporting argument for the appearance of a highly ordered transient phase follows from evaluation of the radial diffuse scattering that is directly related to the short-range disorder and domain orientation disorder in the nanoparticle crystal. Hence, a decrease and increase in the intensity between *111* and *31-1* diffraction spots (black rectangle in the Fig. 3c) reflects a better or worse perfection of the nanoparticle crystal, respectively, in terms of the short-range order and/or domain orientation in [*111*] direction. Integration of the area of the black rectangle is plotted in Fig. 10. Here, one can see the temporal behavior opposite to those shown in Fig. 7d and Fig. 9b with the extreme culminating at ≈125 s where any imperfection of the crystal structure goes obviously to minimum. Simultaneously, the interlayer distance in this intermediate stage of the droplet drying temporarily increases by ~0.1 nm (Fig. 7b). This result is rather striking as the presence of the diffraction spots both in the plane and out of plane of incidence (Fig. 3b) suggests that the nanoparticles have already been in contact before. The result can be understood in view of specific properties of the organic surfactant shell covering the nanoparticle metallic core. For example, the chains of organic surfactant molecules standig up radially from the nanoparticle core could get better stretched in the presence of liquid residua of the organic solvent filling up the rest free spaces between the nanoparticles. This increase of the

hydrodynamic diameter of the nanoparticles would improve temporarily the crystallization process as indicated by GISAXS before the solvent is completely evaporated and the surfactant chains get folded in the dried drop. Hence, a low organic solvent content just before its complete evaporation would promote a solvent-assisted interaction between the surfactant shells of the neighboring nanoparticles resulting in stretching up their molecular chains and the transient structural effect observed. However, a definite interpretation of this effect will require a separate investigation owing to the complexity of the system under study. Similarly, a detailed analysis of the GISAXS pattern of the completely dried nanoparticle crystal based on the 3D short-range order (paracrystal) model is beyond the scope of this paper and can be found elsewhere (Vegso et al. 2014).

Conclusion

The time-resolved GISAXS technique was employed to study kinetics of the spontaneous nanoparticle self-assembly driven by the solvent evaporation. Formation of a 3D nanoparticle crystal with *fcc* symmetry and [*111*] direction oriented along the substrate normal was found after a complete drying of the colloidal solution drop at ≈350 s. The nanoparticle crystal exhibits the short-range order behavior with cumulative disorder except for the time interval of 125-155 s when a non-equilibrium transient phase with long-range order appears. Here, the degree of disorder drops from 3.4 % to 2 % and the coherent domain size increases from 15 to 18 nanoparticle layers. Subsequently, the short-range order is re-established with the final saturated values of 3 % for the disorder and 15 nanoparticle layers for the domain size. A solvent-assisted interaction between the nanoparticle surfactant shells shortly before the solvent is completely evaporated is presumably responsible for the unusual transient effect observed that has direct impact on the quality of the resulting nanoparticle crystal and tailoring its properties.

Acknowledgements

The work was supported by the Slovak Research and Development Agency, projects No. APVV-0125-11 and APVV-0308-11, Grant Agency VEGA Bratislava, project no. 2/0041/11, and Centre of

Excellence SAS FUN-MAT. The support of the SAS-TUBITAK JRP 2013/6 project, COST Action MP1203 and the project "Competence Center for New Materials, Advanced Technologies and Energy", ITMS code 26240220073, supported by the Research and Development Operational Programme funded by the ERDF is also acknowledged.

References

1. Altamura D, Holý V, Siliqi D, Lekshmi IC, Nobile C, Maruccio G, Cozzoli PD, Fan L, Gozzo F, Giannini C (2012) Exploiting GISAXS for the Study of a 3D Ordered Superlattice of Self-Assembled Colloidal Iron Oxide Nanocrystals. Cryst Growth Des 12(11):5505-5512.

2. Atwater HA, Polman A (2010) Plasmonics for improved photovoltaic devices. Nat Mater 9(3):205-213.

3. Buffet A, Rothkirch A, Dohrmann R, Korstgens V, Kashem MMA, Perlich J, Herzog G, Schwartzkopf M, Gehrke R, Muller-Buschbaum P, Roth SV (2012) P03, the microfocus and nanofocus X-ray scattering (MiNaXS) beamline of the PETRA III storage ring: the microfocus endstation. J Synchrot Radiat 19:647-653.

4. Chitu L, Siffalovic P, Majkova E, Jergel M, Vegso K, Luby S, Capek I, Satka A, Perlich J, Timmann A, Roth SV, Keckes J, Maier GA (2010) Modified Langmuir-Blodgett deposition of nanoparticles - measurement of 2D to 3D ordered arrays. Meas Sci Rev 10(5):162-165.

5. Dai Y, Lin B, Meron M, Kim K, Leahy B, Witten TA, Shpyrko OG (2013) Synchrotron X-ray Studies of Rapidly Evolving Morphology of Self-Assembled Nanoparticle Films under Lateral Compression. Langmuir 29(46):14050-14056.

6. Deegan RD, Bakajin O, Dupont TF, Huber G, Nagel SR, Witten TA (1997) Capillary flow as the cause of ring stains from dried liquid drops. Nature 389(6653): 827-829.

7. Dunphy D, Fan H, Li X, Wang J, Brinker CJ (2008) Dynamic Investigation of Gold Nanocrystal Assembly Using In Situ Grazing-Incidence Small-Angle X-ray Scattering. Langmuir 24(19):10575-10578.

8. Eads JL, Millane RP (2001) Diffraction by the ideal paracrystal. Acta Crystallogr Sect A 57:507-517.

9. Elbaz J, Cecconello A, Fan Z, Govorov AO, Willner I (2013) Powering the programmed nanostructure and function of gold nanoparticles with catenated DNA machines. Nat Commun 4

10. Hindeleh AM, Hosemann R (1988) Paracrystals representing the physical state of matter. J Phys C-Solid State 21(23): 4155-4170.

11. Lin ZQ (2012) Evaporative Self-assembly of Ordered Complex Structures, World Scientific Publishing Company, Singapore.

12. Link S, El-Sayed MA (1999) Size and Temperature Dependence of the Plasmon Absorption of Colloidal Gold Nanoparticles. J Phys Chem B 103(21):4212-4217.

13. Macfarlane RJ, Lee B, Jones MR, Harris N, Schatz GC, Mirkin CA (2011) Nanoparticle Superlattice Engineering with DNA. Science 334(6053):204-208.

14. Maier SA, Kik PG, Atwater HA, Meltzer S, Harel E, Koel BE, Requicha AAG (2003) Local detection of electromagnetic energy transport below the diffraction limit in metal nanoparticle plasmon waveguides. Nat Mater 2(4):229-232.

15. Martin MN, Basham JI, Chando P, Eah SK (2010) Charged Gold Nanoparticles in Non-Polar Solvents: 10-min Synthesis and 2D Self-Assembly. Langmuir 26(10):7410-7417.

16. Moscatelli A (2012) Gold nanoparticles afloat Nat. Mater 11(1):8-8.

17. Pohjalainen E, Pohjakallio M, Johans C, Kontturi KS, Timonen JVI, Ikkala O, Ras RHA, Viitala T, Heino MT, Seppälä ET (2010) Cobalt Nanoparticle Langmuir–Schaefer Films on Ethylene Glycol Subphase. Langmuir 26(17):13937-13943.

18. Renaud G, Lazzari R, Leroy F (2009) Probing surface and interface morphology with Grazing Incidence Small Angle X-Ray Scattering. Surf Sci Rep 64(8):255-380.

19. Rong G, Wang H, Skewis LR, Reinhard BRM (2008) Resolving Sub-Diffraction Limit Encounters in Nanoparticle Tracking Using Live Cell Plasmon Coupling Microscopy. Nano Lett 8(10):3386-3393.

20. Rupich SM, Shevchenko EV, Bodnarchuk MI, Lee B, Talapin DV (2009) Size-Dependent Multiple Twinning in Nanocrystal Superlattices. J Am Chem Soc 132(1):289-296.

21. Siffalovic P, Chitu L, Majkova E, Vegso K, Jergel M, Luby S, Capek I, Satka A, Maier GA, Keckes J, Timmann A, Roth SV (2010) Kinetics of Nanoparticle Reassembly Mediated by UV-Photolysis of Surfactant. Langmuir 26(8):5451-5455.

22. Smilgies DM, Heitsch AT, Korgel BA (2012) Stacking of Hexagonal Nanocrystal Layers during Langmuir–Blodgett Deposition. J Phys Chem B 116(20):6017-6026.

23. Smith DK, Goodfellow B, Smilgies DM, Korgel BA (2009) Self-Assembled Simple Hexagonal AB2 Binary Nanocrystal Superlattices: SEM, GISAXS, and Defects. J Am Chem Soc 131(9):3281-3290.

24. Vegso K, Siffalovic P, Jergel M, Weis M, Benkovicova M, Majkova E, Luby S, Kocsis T, Capek I (2012) Silver Nanoparticle Monolayer-to-Bilayer Transition at the Air/Water Interface as Studied by the GISAXS Technique: Application of a New Paracrystal Model. Langmuir 28(25):9395-9404.

25. Vegso K, Siffalovic P, Weis M, Jergel M, Benkovicova M, Majkova E, Chitu L, Halahovets Y, Luby S, Capek I, Satka A (2011) In situ GISAXS monitoring of Langmuir nanoparticle multilayer degradation processes induced by UV photolysis. Phys Status Solidi A-Appl Mat 208(11):2629-2634.

26. Vegso K, Siffalovic P, Jergel M, Majkova E, Kocsis T, Benkovicova M, Luby S, Capek I, Perlich J, Roth SV (2014) Application of the paracrystal model to GISAXS analysis of the 3D self-assembled nanoparticle crystals. Phys Status Solidi B 251(6):1169–1177.

27. Willingham B, Link S (2011) Energy transport in metal nanoparticle chains via sub-radiant plasmon modes. Opt Express 19(7):6450-6461.

Figures

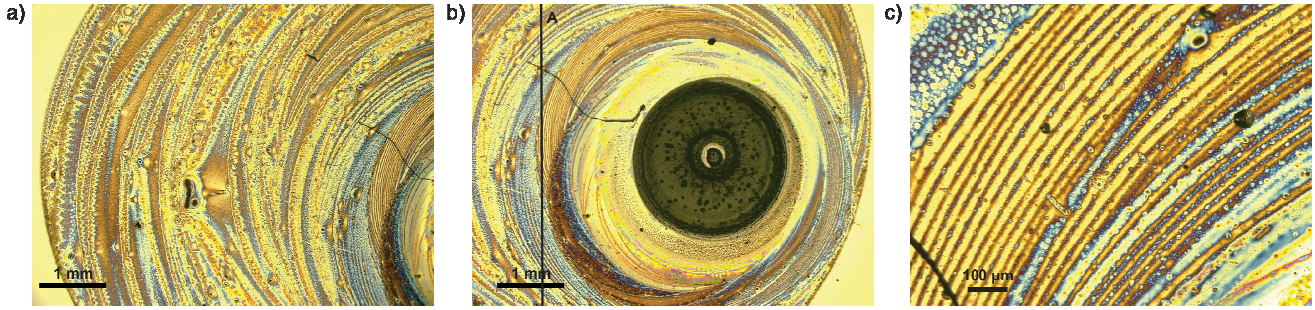

Figure 1. Optical microscopic images of a) left margin and b) center of dried nanoparticle droplet. c) The detail view on concentric ring deposits forming after solvent evaporation.

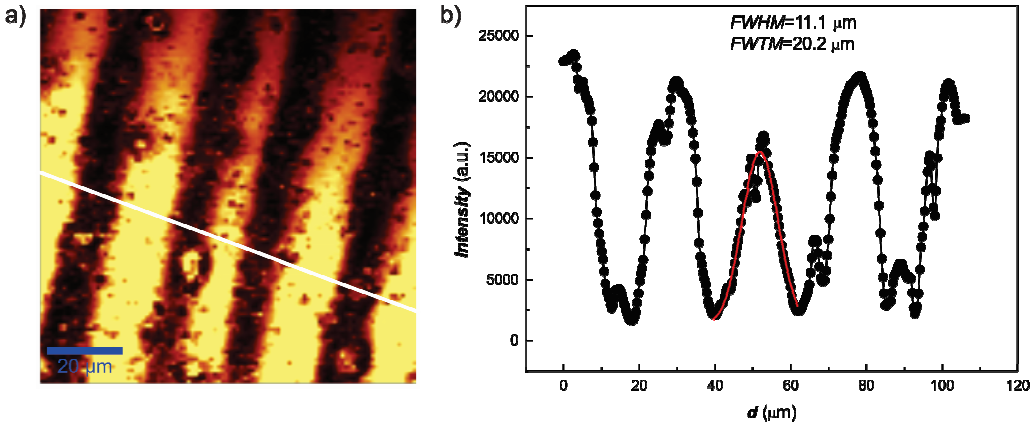

Figure 2. a) Confocal image of multiple ring deposits and b) the cross-section recorded along white line in the Fig. 2a.

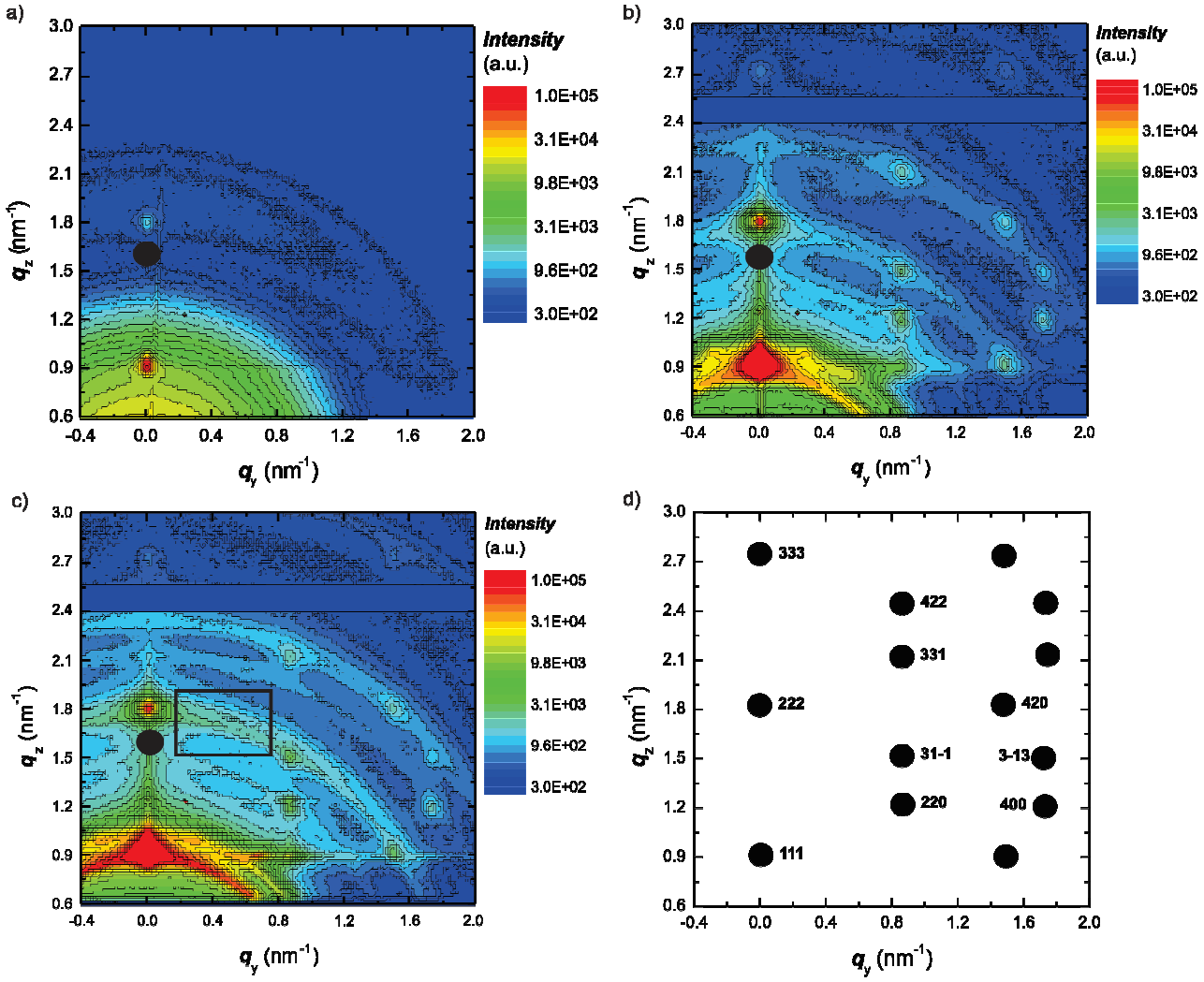

Figure 3. GISAXS patterns obtained at a) initial (0-5 s), b) intermediate (120-125 s) and c) final (300-305 s) stages of the drop drying that reveal diffraction spots with the face-centered cubic (*fcc*) symmetry indexed in d). The black rectangle in c) defines the integration area for the radial diffuse scattering shown in Fig. 10 (see the text).

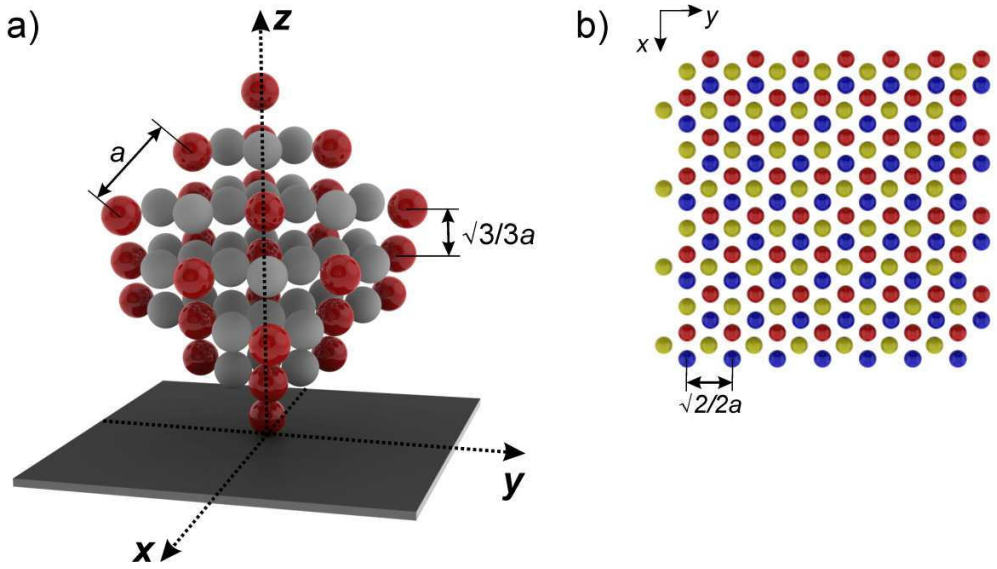

Figure 4. a) The *fcc* nanoparticle crystal with [*111*] direction oriented along the substrate normal where a is the lattice parameter and $\sqrt{3}/3a$ is the interlayer distance. b) Top-view of the crystal showing *ABC* stacking typical for *fcc* structure with the in-plane interparticle distance equal to $\sqrt{2}/2a$. The blue, yellow and red colors represent the first, second and third layer of *ABC* stacking, respectively.

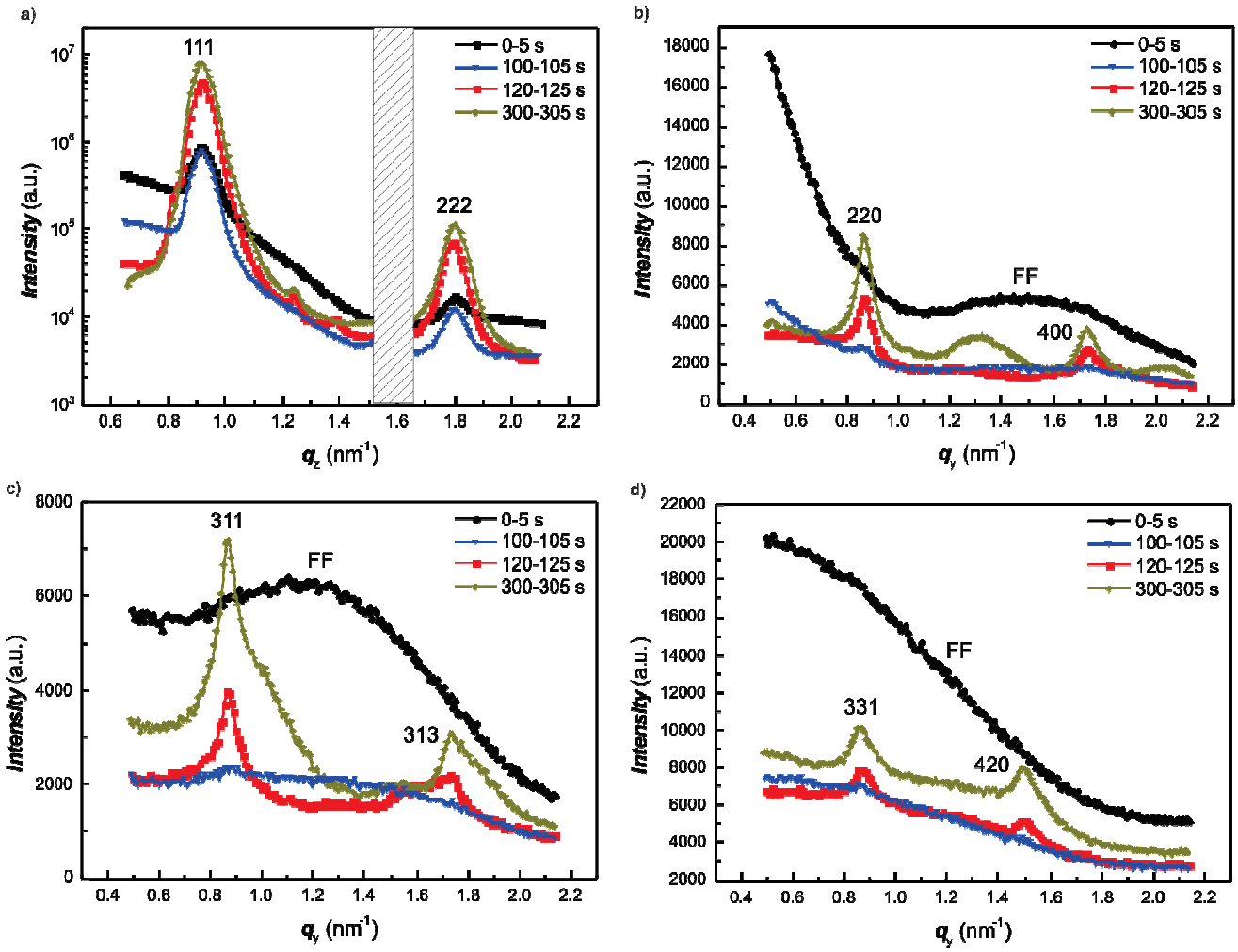

Figure 5. Evolution of Bragg peaks a) in the plane and b) out of the plane of incidence of X-rays obtained from integration of the GISAXS patterns around $q_y = 0$ nm^{-1} and in selected q_z intervals, respectively, at different times. Mark FF denotes the form factor of the nanoparticles.

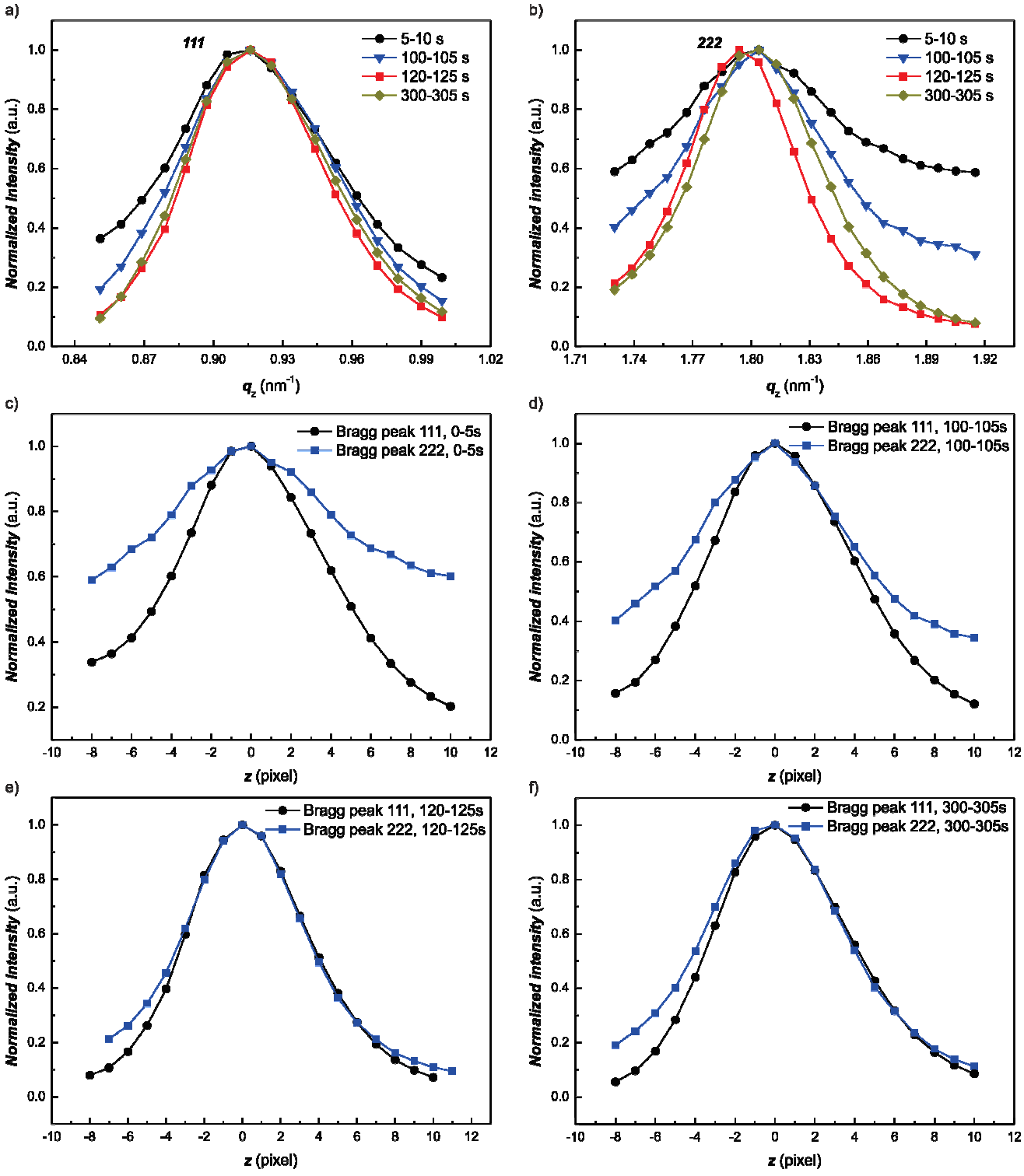

Figure 6. Evolution of the normalized intensity distributions in a) 111 and b) 222 Bragg peaks at different times. The direct comparison of normalized intensity distributions in 111 and 222 Bragg peaks at a) 0-5s, b) 100-105 s, c) 120-125 s and d) 300-305 s times, respectively.

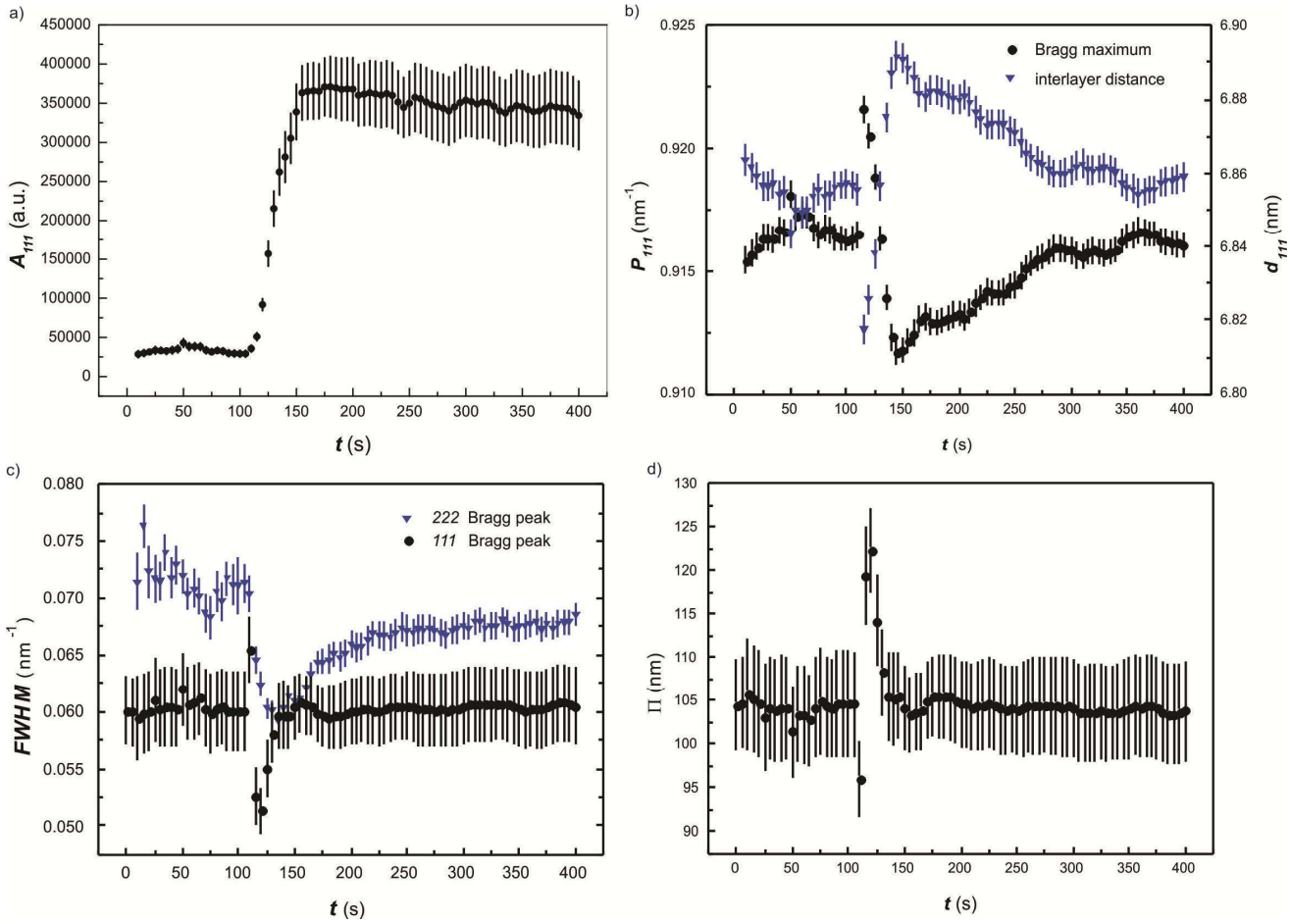

Figure 7. Temporal evolution of a) the area under *111* Bragg peak, b) the position of maximum of *111* Bragg peak and the interlayer distance, c) FWHM of *111* and *222* Bragg peaks and d) the size of coherent domain in [*111*] direction derived from FWHM of *111* Bragg peak.

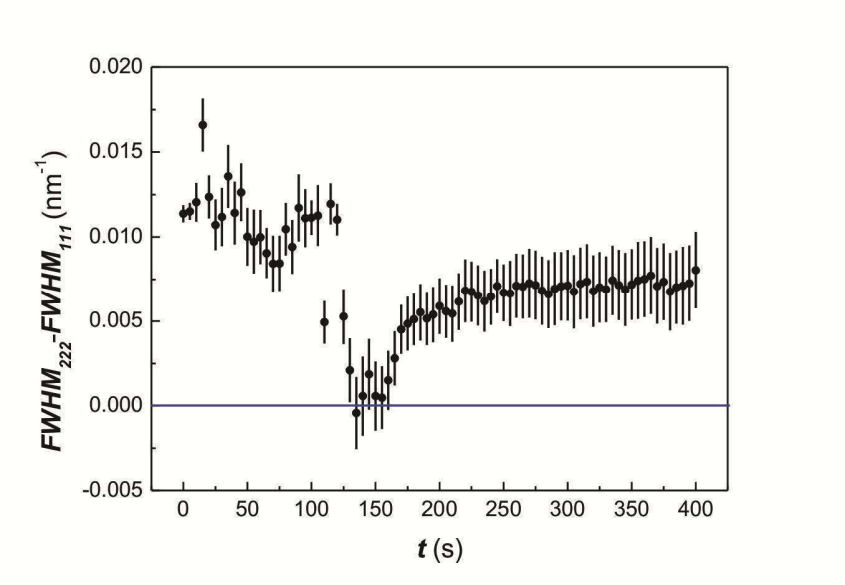

Figure 8. Temporal evolution of the difference between FWHM values of *111* and *222* Bragg peaks.

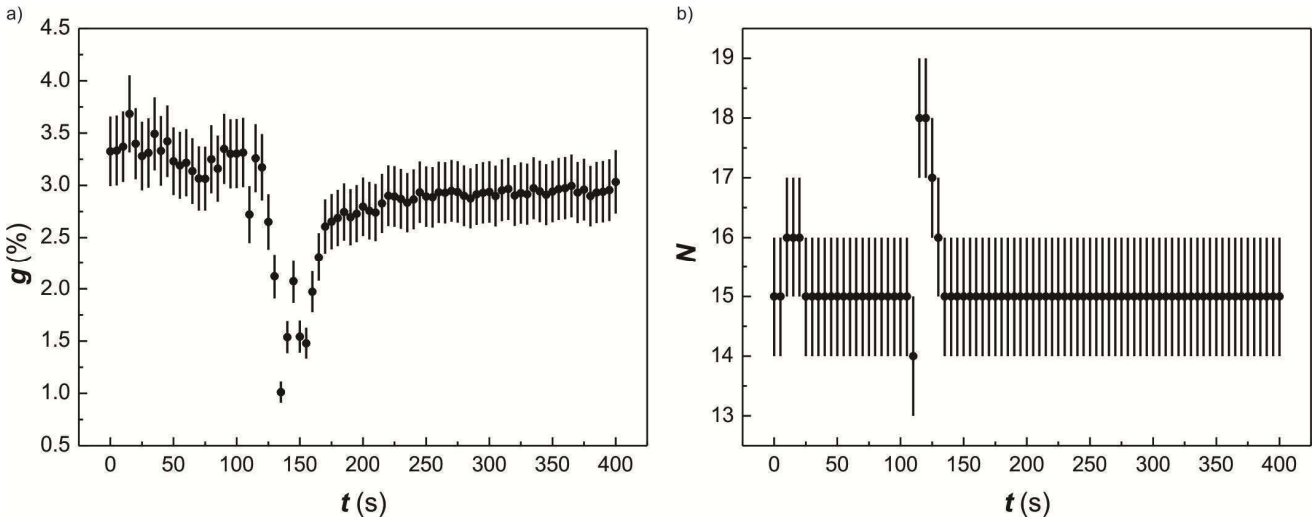

Figure 9. Temporal evolution of a) the paracrystal disorder and b) the size of coherent domain in [*111*] direction derived from FWHM values of *111* and *222* Bragg peaks and the interlayer distance d_{111}.

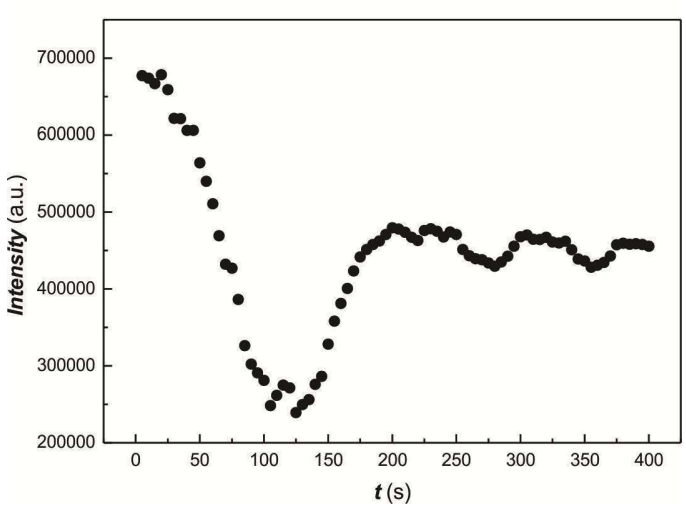

Figure 10. Temporal evolution of the radial diffuse scattering obtained from integration of the GISAXS patterns between *222* and *31-1* diffraction spots at different times (see the black rectangle in Fig. 3c).